# Cavity electro-optic circuit for microwave-to-optical conversion in the quantum ground state

Wei Fu, Mingrui Xu, Nianwen Liu, Chang-Ling Zou, Changchun Zhong, Xu Han, Mohan Shen, Yuntao Xu, Risheng Cheng, Sihao Wang, Liang Jiang, and Hong X. Tang, Tang, Tang, Now Haven, Connecticut 06520, USA

Pritzker School of Molecular Engineering, University, New Haven, Connecticut 06520, USA

Yale Quantum Institute, Yale University, New Haven, Connecticut 06520, USA

(Received 15 December 2020; accepted 25 March 2021; published 10 May 2021)

In the development of microwave-to-optical (MO) quantum transducers, suppressing added noise induced by the optical excitation remains a major challenge. Here we report an integrated superconducting cavity electro-optic circuit based on single crystalline thin-film aluminum nitride of ultralow microwave and optical losses. We demonstrate efficient bi-directional MO conversion at milli-Kelvin temperatures, with near-ground state microwave thermal excitation ( $\bar{n}_e = 0.09 \pm 0.06$ ), despite the peak power of the optical drive exceeding the cooling power of the dilution refrigerator mixing chamber. Our dynamical study further reveals different light-induced noise generation mechanisms and provides crucial guidelines for optimizing electro-optic circuits in future hybrid microwave-optical quantum links.

DOI: 10.1103/PhysRevA.103.053504

### I. INTRODUCTION

In pursuit of quantum microwave-to-optical (MO) conversion, hybrid superconducting-photonics systems operated in cryogenic conditions have drawn wide attention as a building block of the envisioned future quantum network [1–5]. Among many promising platforms including atomic spin ensembles [6,7], rare-earth doped crystals [8,9], ferromagnetic magnons [10-12], electro-opto-mechanics [13-20], and bulk electro-optics [21,22], integrated cavity electro-optics [23–28] stands out as a particularly attractive device architecture. Harnessing the Pockels effect, integrated electro-optical platforms offer advantages including tunability, scalability, and high power handling capability since the device can be embedded in a planar circuit without any free-standing structures. A recent work based on aluminum nitride (AlN) cavity electro-optics has demonstrated electromagnetically induced transparency and a state-of-art conversion efficiency of 2% at 1.7 K [25]. Orders of magnitude of improvement in electro-optical coupling strength becomes possible with the recent advance in material platforms including Lithium niobate [26,27,29] and barium titanate [30].

For quantum transduction applications, it is crucial to obtain both high electro-optical coupling rates and low thermal fluctuations, which is assisted by an intense optical parametric drive at the milli-Kelvin temperature [14,16,22,31,32]. This is particularly challenging because the optical drive could dissipate significant amount of heat in the dilution refrigerator that easily exceeds its cooling power at the base temperature, raise the device temperature and induce extra microwave noise through photon absorption by dielectrics and superconductor [33–36]. Promising progress has

been made by recent demonstrations of MO conversion with ground-state electro-opto-mechanics [17,20] and bulk electro-optics [22]. However, to achieve close-to-unitary conversion efficiency, which is required for quantum state transduction [37], implementation of stronger parametric optical drives in a microresonator system seems to be inevitable. Therefore, a systematic understanding of thermal dynamics of the microwave resonance in a hybrid superconducting-photonic system, which may shed light on further suppressing the microwave noise in presence of a strong optical drive, is highly anticipated.

In this work, we study a near-ground-state integrated electro-optical MO converter mounted in a dilution refrigerator at milli-Kelvin temperatures, and its microwave thermal excitations induced by strong pulsed optical drives. We achieved bidirectional direct MO photon conversion with an internal efficiency 0.15%. Moreover, the microwave thermal noise from the device microwave port is calibrated through precise noise thermometry assisted by an ultralownoise traveling wave amplifier [38], as illustrated in Fig. 1(a). Pulsed optical drives is employed to suppress the microwave noise while achieving high conversion efficiency. Compared with the thermal occupancy of the microwave mode under continuous-wave (cw) optical drives, the pulsed optical drives allow around 30 dB higher peak pump power, while maintaining the same level of thermal excitations. In the presence of a pulsed optical drive with a peak power of -11.4 dBm (72  $\mu$ W) in the waveguide, which exceeds the dilution refrigerator's cooling power of 50  $\mu$ W at the base temperature around 40 mK, the microwave mode occupancy is observed to be  $0.09 \pm 0.06$ , which corresponds to  $92 \pm 5\%$  groundstate probability. Finally, dynamical microwave noise study revealed different light-induced microwave noise sources and suggests that in our system, the dominating noise source is caused by the superconductor absorption of stray light

<sup>\*</sup>hong.tang@yale.edu

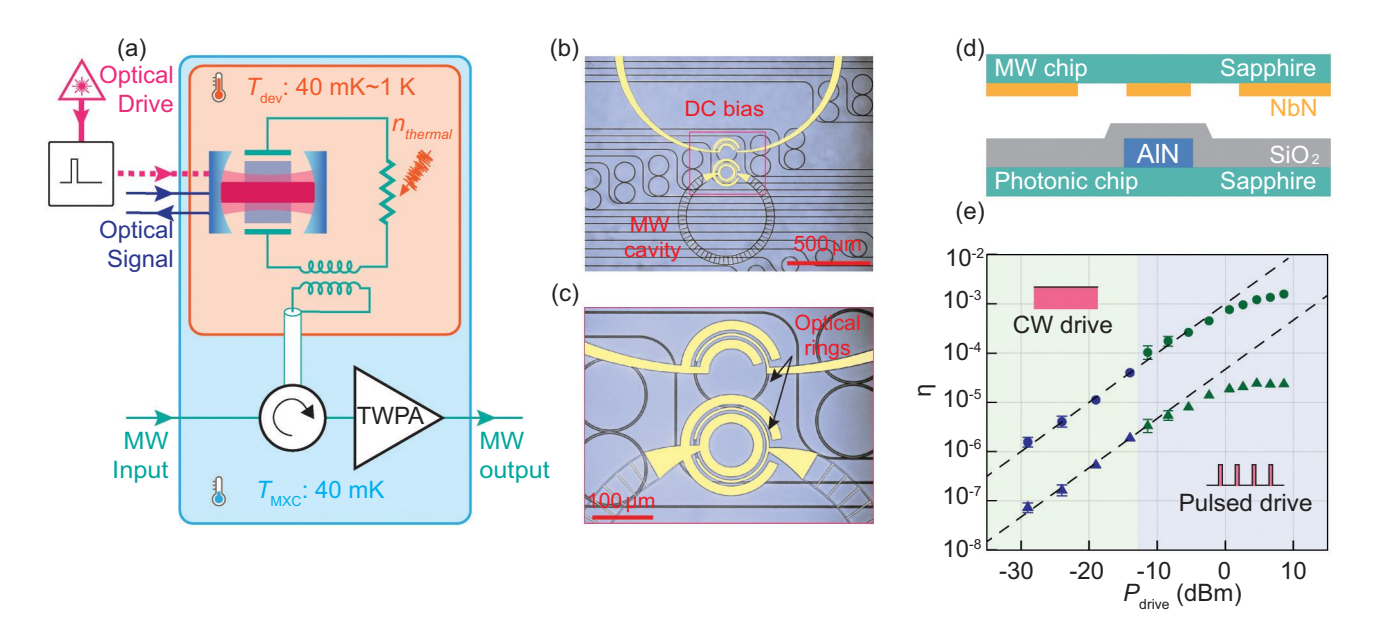


FIG. 1. (a) A schematic of the experiment: an electro-optical (EO) transducer is installed in a milli-Kelvin environment. An optical drive is sent to the device to enhance parametric EO coupling but also inevitably introduces extraneous noise. A traveling wave amplifier (TWPA) is used to provide low-added noise readout of the microwave signal and noise from its output port. (b) and (c) are images of the EO transducer device. (d) Schematic of the flip-chip design. (e) Calibrated microwave-to-optical conversion efficiency as a function of optical drive power in the photonic waveguide. The internal efficiency is represented by the round dots and the on-chip efficiency is represented by the triangular dots. The blue dots are data measured with the continuous-wave (cw) scheme; the olive dots are data measured with the pulsed scheme, as illustrated by the inset cartoons. Error bars represent the fitting error. The dashed line shows theoretically predicted conversion efficiency extrapolated from the cw regime.

scattered from the chip-fiber interface. Such a mechanism creates an effective thermal bath with a fast response time much less than the 200 ns measurement time constant. The study of light-induced microwave noise provides guidelines for further suppressing microwave noise in cavity electro-optic systems, which is essential for a variety of quantum applications that interface microwave and telecommunication frequencies.

#### II. DEVICE DESIGN AND IMPLEMENTATION

The electro-optical transducer studied in this work utilizes a triple-resonant scheme, where a microwave mode is coupled to two optical modes via the Pockels effect. In our previous implementations [25], a pair of hybrid, dispersion-engineered transverse electric (TE) or transverse magnetic (TM) modes are utilized to satisfy electro-optical phase matching. Here we adopt a double-ring structure [26–28] to allow on-chip tuning of optical modal splitting by applying a DC voltage through integrated DC bias electrode. Figures 1(b) and 1(c) present images of the transducer. The double-ring structure supports hybridized symmetric and antisymmetric TE optical modes for optical drive (a mode) and signal (b mode). A tunable ouroboros LC resonator [39] made of niobium nitride (NbN) supports the microwave mode (c mode), in which the capacitor is composed of three concentric ground-signal-ground electrodes. As a result, the electric field in the proximity of the middle electrode is perpendicular to the surface of the bottom microring. The inductor part consists wires with high kinetic inductance which provides resonant frequency tunability [39].

In this electro-optical system, the interaction Hamiltonian is  $H_{\text{int}} = \hbar g_0 (ab^{\dagger}c + a^{\dagger}bc^{\dagger})$ , where a, b, and c are the

annihilation operators for the optical drive mode, optical signal mode, and microwave mode, respectively, and  $g_0$  is the vacuum electro-optical coupling rate due to Pockels effect. Pumping the lower frequency optical mode a enables coherent conversion between the optical mode b and the microwave mode c. When the frequency difference between the optical modes matches the microwave mode's frequency, the peak on-chip conversion efficiency can be expressed as [25]

$$\eta = \eta_{\rm c} \eta_{\rm b} \eta_{\rm int} = \frac{\kappa_{\rm c,ex}}{\kappa_{\rm c}} \frac{\kappa_{\rm b,ex}}{\kappa_{\rm b}} \frac{4C}{(1+C)^2},\tag{1}$$

where  $\eta_b$  ( $\eta_c$ ),  $\kappa_{b,ex}$  ( $\kappa_{c,ex}$ ), and  $\kappa_b$  ( $\kappa_c$ ) are the extraction ratio, external loss rate, and total loss rate of the optical mode b (microwave mode c).  $\eta_{int}$  is the internal-conversion efficiency. The electro-optical cooperativity  $C = \frac{4n_{drive}g_o^2}{\kappa_b\kappa_c}$  is resonantly enhanced by the optical drive which excites  $n_{drive}$  intracavity photons.

The microwave and photonic chips are fabricated independently and then assembled through flip-chip bonding, as illustrated in Fig. 1(d). The photonic circuit is fabricated from a 1- $\mu$ m-thick crystalline AlN layer grown on a sapphire substrate, and is then capped by 1.5- $\mu$ m-thick silicon dioxide cladding prior to the waveguide facet cleavage. The microwave resonator and the DC bias electrode are patterned from a 50-nm NbN thin film deposited on a sapphire substrate. To maximize the overlap between the microwave and optical modes for a larger  $g_0$ , the two chips are flip-chip assembled via a home-built bonding station with an in-plane alignment error less than 1  $\mu$ m. With flip-chip implementation, the microwave resonator can be prepared on a low-loss sapphire substrate

while the optical chip can be separately fabricated and annealed at high temperatures to further suppress optical loss. This could potentially lead to lower converter added noise because of less optical photon absorption. Fibers are glued to the side of the chip to send and collect light. The total insertion loss between the input and output fiber connectors outside the refrigerator is calibrated to be around 12 dB. A coaxial cable terminated with a hoop antenna is employed to inductively couple with the microwave mode for input and readout. To shield external radiation and provide thermal anchor, we house the device under test (DUT) in a copper box, which is installed in the MXC of a dilution refrigerator.

When a resonant optical drive is sent to the device through the fiber, a significant portion of the input optical power, which is around 50% based on a room-temperature calibration, is not coupled to the waveguide and scattered off the chip-fiber interface. These uncoupled photons, when absorbed by the device assembly, lead to heating of the chip as well as the packaging. The coupled light propagates along the waveguide and eventually dissipates in the microring, inducing local heating in the cavity. Heat generated in the device is dissipated through thermal contact between sapphire substrate and the copper housing, which is well thermalized to the MXC.

### III. DEVICE PERFORMANCE UNDER PULSED DRIVE

To parametrically enhance the electro-optical coupling without excessively heating up the device as well as the MXC, we implement a pulsed drive scheme. As illustrated in Fig. 1(a), a cw laser from a tunable laser diode is modulated by an electrical pulse via an acousto-optic modulator (AOM), of which rise and fall time is 35 ns, before being sent into the device. Upon decreasing the duty cycle of the pulse signal, we essentially reduce the heat load to the device while maintaining the peak intracavity photon number. In the experiments described below, we use pulses with 0.2% duty cycle and 1 ms period. Thanks to the large extinction of the AOM, the optical drive power on-off ratio is over 50 dB. As a result, the heating caused by the leaked optical drive while off-duty can be neglected. With such a pulsed drive scheme, we can send a laser drive with 0 dBm peak power while the MXC temperature only rises 1 mK from the base temperature.

By measuring the spectra of the complete transducer's scattering matrix, we calibrated the conversion efficiency with both cw and pulsed drives of different powers [40]. Both internal efficiency (round dots) and on-chip efficiency (triangular dots) are shown in Fig. 1(e), where the blue dots represent efficiencies measured with cw drives, and the olive dots represent efficiencies measured with pulsed drives, as illustrated by the inset cartoons. When pumping with 4.6 dBm pulsed drive, the highest efficiency is observed to be  $\eta = 2.4 \times 10^{-5}$  with a bandwidth of 2.9 MHz, which corresponds to an internal efficiency  $\eta_{\text{int}} = 0.12\%$  and an electro-optical cooperativity  $C = 3 \times 10^{-4}$ . Limited by the extraction ratios of both the optical and microwave mode, the on-chip efficiency is between one and two orders of magnitude lower than the internal efficiency. The dashed line shows theoretically predicted conversion efficiency based on Eq. (1) with the coefficient  $g_0 =$ 42 Hz and and microwave Q extracted from measurements

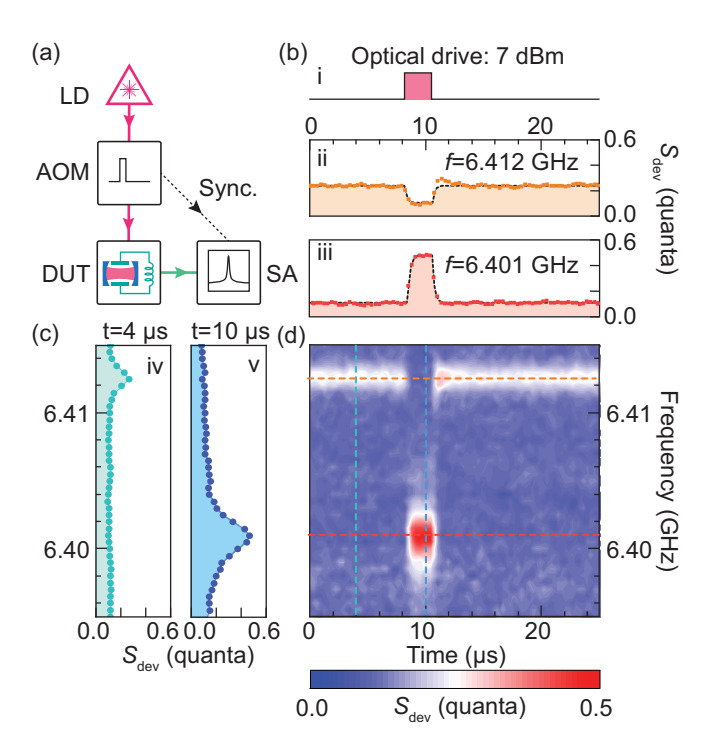


FIG. 2. (a) Simplified diagram of the experiment setup. LD: Laser diode. AOM: acousto-optic modulator. DUT: device under test. SA: spectrum analyzer or a lock-in amplifier that measures the noise spectrum. A cw laser is modulated with a pulse signal via an AOM before being sent into the device. The microwave noise is amplified by a low-noise amplification chain before being recorded by a lock-in amplifier, which is represented by a spectrum analyzer in the diagram. The heat map (d) shows the time evolution of the noise spectrum. The time traces of noise power spectral density at original resonance frequency (ii) and shifted frequency (iii) are shown in panel (b), compared with the illustrated optical drive power in panel (i). Panel (c) shows the snapshots of power spectral density when the pulsed laser drive is off (iv) and on (v). Data in panels (b) and (c) are cross sections of panel (d) marked in correspondingly colored dashed lines.

with a -25.4 dBm cw drive. The efficiency starts to deviate from the theoretical expectation at around -6 dBm. This is a result of a decreased microwave intrinsic quality factor due to quasiparticles generated via superconductor absorption of optical photons [33–36]. In the higher-power regime (>0 dBm), the efficiencies deviate more from the theoretical value, possibly due to parasitic nonlinear effects in the ring resonator such as the thermal-optic effect [41].

To study the dynamical noise performance of the device, we implement a fast precision measurement to monitor the power spectral density of the microwave side output noise as illustrated in Fig. 2(a). For better noise photon resolution, a traveling-wave amplifier with GHz-level bandwidth [38] is utilized to achieve a low added noise readout chain. To characterize the absolute gain and added noise of the output chain, a noise thermometry calibration was performed and revealed the output line added noise as around four quanta at the frequencies of interest [40], which is calibrated out in the following results. The noise power measurement is performed

with a lock-in amplifier (LIA) with a low-pass filter bandwidth of 700 kHz, which corresponds to a time constant  $t_c = 202$  ns.

Measurement results at 7 dBm pulsed optical drive is shown in Fig. 2. The heat map [Fig. 2(d)] depicts the time evolution of the light-induced noise power spectrum. A consistent background noise of around 0.11 quanta is observed across the entire frequency range of interest, which is also manifest in Figs. 2(b) and 2(c). During the light-off period, a peak on the noise spectrum [Fig. 2(c)(iv)] at the microwave resonant frequency 6.412 GHz indicates a finite thermal excitation. In comparison, during the light-on period, as shown in Fig. 2(c)(v), the superconducting resonant frequency redshifts 11 MHz, and the resonance linewidth is broadened. Moreover, the noise peak rises, indicating a stronger thermal excitation of the microwave mode. The temporal evolution of the noise power spectral density at these two center frequencies are captured in Fig. 2(b). In the light-off period, Fig. 2(b)(ii) suggests that the microwave thermal excitation is relatively stable, it could be attributed to a thermal bath with a large time constant. From Fig. 2(b)(iii), it is evident that during the light-on period, a new thermal equilibrium is established. The rising and falling edges of the measured transition agree well with the theoretical exponential functions (dashed curves), of which the time constant is equivalent to the measurement time constant  $t_c = 202$  ns. This suggests that the actual transition time, which includes the resonance frequency shift as well as the heating when the light is turned on should be much shorter than 200 ns.

The fast frequency shift and linewidth broadening when light is shined on the superconducting material are typically attributed to the superconductor absorption of photons [33–36]. During this process, the photon absorption breaks Cooper pairs, generates quasiparticles, and consequently increases the kinetic inductance and induces extra dissipation in the superconductor. Our results imply that for NbN the quasiparticle recombination time is much faster than 200 ns at 40 mK regime [35,36].

From the microwave output noise power spectra, we can infer the light-induced effective thermal bath occupancy as well as microwave mode thermal excitations. As introduced in detail in Ref. [42], the output noise spectrum can be written as

$$S_{\text{dev}}(\omega) = \mathcal{R}(\omega)\bar{n}_{\text{ex}} + [1 - \mathcal{R}(\omega)]\bar{n}_{\text{en}} + \Delta\bar{n}_{\text{out,add}},$$
 (2)

in which  $\mathcal{R}(\omega) = 1 - \kappa_{c,in} \kappa_{c,ex} / [(\kappa_c/2)^2 + (\omega - \omega_0)^2]$ . Here the first and second terms are contribution from the external bath and intrinsic bath, respectively, and  $\Delta \bar{n}_{out,add}$  represents the additional output line added noise induced by light.  $\kappa_{c,in}$  and  $\kappa_{c,ex}$  are the coupling rates to the intrinsic and the external decay channels, and  $\omega_0$  is the angular resonant frequency of the resonator.  $\bar{n}_{en}$  and  $\bar{n}_{ex}$  are the respective bath occupancy of the intrinsic bath and the external bath.

By fitting each noise spectrum to Eq. (2), the intrinsic and external thermal bath occupancy can be found. Given both bath occupancies, the microwave mode thermal excitation can be calculated as the weighted average of the two thermal baths

$$\bar{n}_{\rm e} = \frac{\kappa_{\rm c,in}\bar{n}_{\rm en} + \kappa_{\rm c,ex}\bar{n}_{\rm ex}}{\kappa_{\rm c,in} + \kappa_{\rm c,ex}}.$$
 (3)

Figure 3(b) shows microwave noise power spectra in the light-on period of different pulsed drives. In comparison, noise power spectra with different cw optical drive are plotted in Fig. 3(a). Solid lines in both Fig. 3(a) and 3(b) are the theoretical fit to Eq. (2) with the coupling parameters ( $\kappa_{ex}$ and  $\kappa_{in}$ ) each independently evaluated from the reflection spectrum by probing with a weak coherent tone. Significant frequency shifts of the microwave resonance is observed when a strong pulsed drive is applied due to optical absorption by superconductor. It is worth noting that a weak background noise (shaded in gray) is observed in power spectra when a strong cw or pulsed optical drive is applied. In the pulsed measurement, the background noise power stays consistent during the entire measurement time span, indicating its large time constant compared with the pulse period 1 ms. Further investigation is needed to identify the source of the excess background noise. It could be attributed to the heated external bath of the superconducting resonator, or increased added noise of the amplification chain due to the optical excitation.

Based on the fitted microwave noise power spectra, the average thermal occupancies of the superconducting modes when driven with different optical pumps are plotted in Fig. 3(c). Due to the uncertain nature of the background noise that appears in some higher-power cw and pulsed measurements, lower bound (orange and purple) and upper bound (green and blue) of the microwave mode occupancy are provided. The upper bound values are obtained by considering the background noise as the heated external bath  $\bar{n}_{ex}$  of the superconducting resonator, which contributes to the microwave thermal occupancy; the lower bound corresponds to the case when the background noise is considered as additional added noise in the output chain  $\Delta \bar{n}_{\text{out,add}}$ , which does not contribute to the microwave thermal excitation. Fitting errors are also marked on each data point. When a pulsed drive of -11.4 dBm peak power is applied in the waveguide, the microwave mode occupancy  $\bar{n}_{\rm e} = 0.09 \pm 0.06$ , corresponding to a mode which is at its quantum ground state with 92  $\pm$ 5% probability. The corresponding on-chip conversion efficiency is  $\eta = 3.3 \times 10^{-6}$ . When increasing the pulsed drive peak power, the thermal occupancy scales approximately in proportion (power = 1.03) to the pulsed drive power. With 4.6 dBm peak drive power, where the converter shows the highest on-chip efficiency, the microwave mode occupancy is increased to  $\bar{n}_{\rm e}=1.8\pm0.3$ . Compared to the cw drive, the pulsed optical drive allows a larger peak power to boost the electro-optical coupling rate by around three orders of magnitudes, while maintaining close-to-ground-state microwave resonance. The different scaling trend of thermal excitation to power between cw and pulsed operation suggests different heating mechanisms.

## IV. HEATING MECHANISM ANALYSIS

To gain insight regarding the underlying heating mechanisms, we further analyze the time evolution of the noise spectrum with various optical drive powers. Figure 2 suggests two types of effective intrinsic baths with distinct time constants. The first is a slow-responding effective bath, which is responsible for the microwave noise during the light-off

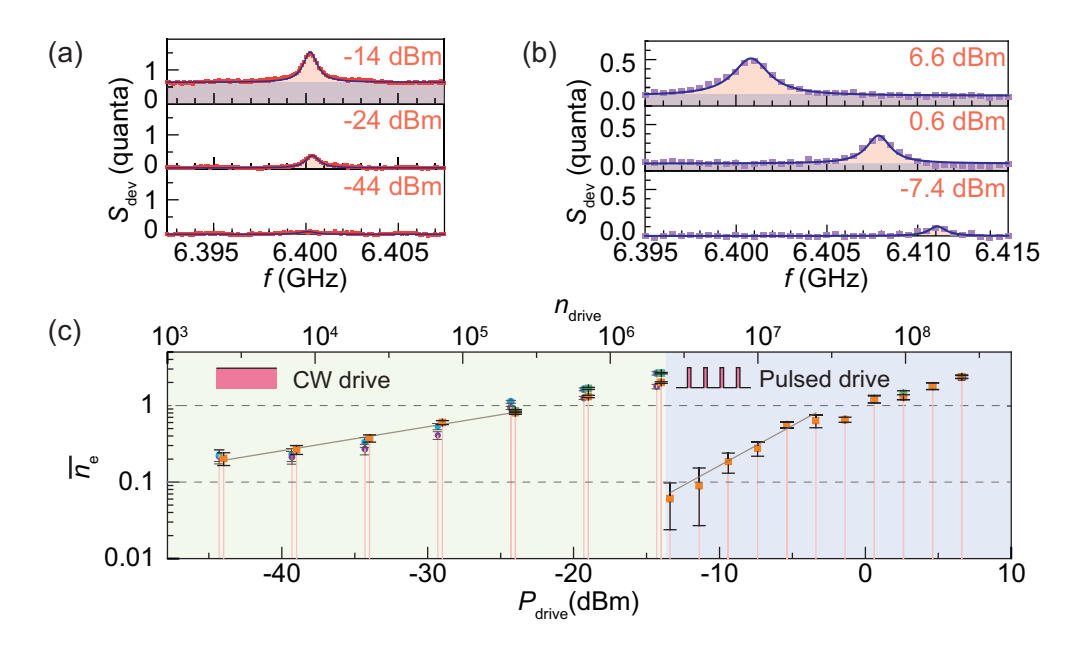


FIG. 3. Panels (a) and (b) shows noise power spectra  $S_{\text{dev}}$  when cw and pulsed drives of different power are applied. The solid curve is the theoretical fit with coupling parameters independently characterized. Panel (c) summarizes the microwave mode thermal occupancies  $\bar{n}_{\text{e}}$  at different optical drives. The x axis represents the power of the cw drive or the peak power of the pulsed drive. Green data points, if visible, represent the upper bound of the occupancy given the uncertain nature of the observed noise background in the spectrum. Accordingly, the orange data points represents the lower bound of the occupancy. Continuous-wave results from a different cool down are shown as the purple (lower bound) and blue (upper bound) data points.

period. With no discernible change in slow bath occupancy for the entire pulse period, we can conclude that its time constant is much larger than the period of the pulsed drive T = 1 ms. The second type is a fast-responding thermal bath with a ramp-up time much quicker than our data-acquisition time constant 202 ns, which contributes to the extra noise in the microwave resonator when the light is on. The slow-responding bath can be attributed to heating due to optical absorption by dielectrics and other materials that stray light shines on. The fast-responding effective bath, on the other hand, likely originates from quasiparticles generation and recombination due to superconductor absorption of optical photons. Another possible contribution to the fast thermal bath is localized dielectric heating in the optical cavity. Compared to the slow bath, the fast bath is harder to manage in an electro-optical system with a strong optical drive, because it cannot be suppressed by optimizing the pulsed drive configuration. Figure 4(a) plots the microwave effective bath occupancy of the steady states when the optical drive is on and off. According to the analysis above, the blue area represents the slow-responding bath occupancy and the pink area represents the contribution from the fast-responding effective bath. The result shows that the contribution of the fast-responding effective bath is initially smaller than that of the slow-responding bath with the lowest pulsed drive power but is accountable for the majority of microwave noise in the higher pulsed drive power regime as it scales faster with the drive power.

The next subject we study is the contribution to the microwave thermal excitation from different optical photon sources, among which we mainly focus on two categories: The cavity photons that are dissipated in the microring and those stray photons scattered off the chip-fiber interface. For this device under test, based on the calibration at room temper-

ature, 50% of light in the fiber is not coupled to the waveguide and scattered off the chip-fiber interface. The rest is coupled to the waveguide and mostly dissipated in the microring for a resonant drive because of the critical-coupling condition, or, for a detuned drive, transmitted in the low-loss waveguide and then coupled back to the fiber. To discriminate the impact of the optical photons scattered off the chip-fiber interface, we characterize microwave noise when applying a nonresonant optical drive. In contrast to a resonant drive, a nonresonant drive does not launch cavity photons nor generate local heat in the microring. Figure 4(b) shows light-on microwave intrinsic effective bath occupancy with 0.6 dBm pulsed drives that are resonant, detuned by one-linewidth and completely detuned. The difference in thermal bath occupancy when applying the resonant and the detuned drive is  $17\% \pm 7\%$ . This results suggest that, despite the large mode overlap between the microwave and the optical modes, optical cavity photons, which introduce dielectric heating as well as local radiation absorbed by superconductor, only contribute approximately 17% of the microwave thermal excitation. The leading factor of the microwave mode heating is thus concluded to be superconductor absorption of stray light which are scattered off the chip-fiber interface.

# V. DISCUSSION AND PERSPECTIVES

Admittedly, for the very device studied in this work, even with reduced microwave noise using the pulsed drive scheme, practical quantum applications still remains elusive. One major limitation is the relatively weak electro-optical coupling, which leads to insufficient conversion efficiency between the microwave mode and optical mode, because of the undesired gap between the superconducting and photonic chip

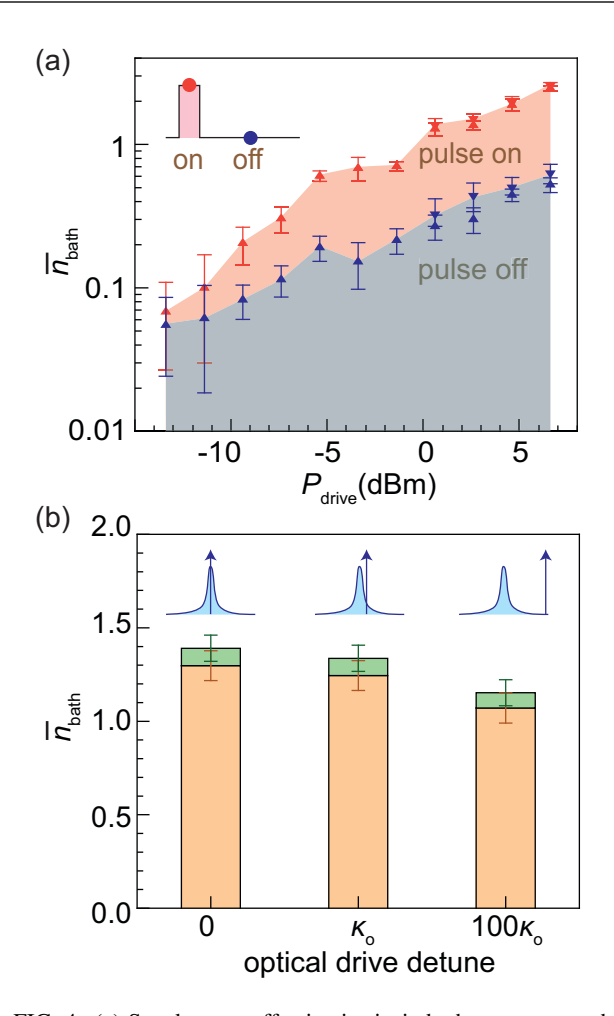


FIG. 4. (a) Steady-state effective intrinsic bath occupancy when the pulsed drives are on and off duty. Lower bound and upper bound of some data points are provided as the triangle pointing up and down, respectively, due to the presence of the background noise of which origin is not known to us yet. (b) Microwave intrinsic bath occupancy when applying 0.6 dBm optical drives that are on-resonance, detuned by one linewidth and completely detuned. Lower bound (orange) and upper bound (green) are provided.

(estimated to be 14  $\mu$ m, see Ref. [40]). To achieve a larger vacuum electro-optical coupling coefficient, one can use better bonding technique or employ the single-chip approach [25], which promises approximately 1 order of magnitude enhancement. Switching to material platforms with higher Pockels coefficient such as lithium niobate and barium titanate can potentially bring about orders of magnitude improvement [27–30]. Applying stronger optical pumps could also parametrically enhance the electro-optical coupling strength, while it demands improved device power handling capability beyond what is achieved here.

Regarding the light-induced microwave noise, our work revealed two types of thermal bath with distinct time constants. The slow responding bath, which is determined by the average optical drive power, could be further suppressed by using lower duty cycles at a given peak drive power. The fast responding bath, which is a more dominant factor at higher optical drive powers, is relatively insensitive to the change of pulsed drive configuration within one order of magnitude, because the new steady state is rapidly established within 200 ns after the drive is turned on. Separate tests with T = 16 ms and duty cycle of 0.2% yields similar results to that with T = 1 ms and 0.2% duty cycle. To further reduce the fast responding bath occupancy at a given optical pump power, possible solutions include spatially distancing the chip-fiber interface from the superconducting resonator, creating proper shield to block stray light from the chip-fiber interface, and providing better thermal dissipation channels to the superconducting material, for example immersing the device in superfluid helium [25]. When adopting an over-coupled configuration for the microwave resonator, the microwave resonance could also be radiatively cooled by exchanging heat with a cold bath through the microwave waveguide [42,43].

To achieve a finite quantum capacity for a microwave-tooptical transducer working as a bosonic channel, it is required to have at least 50% conversion efficiency while maintaining low added noise [44-46], which means approximately three orders of magnitude of improvements needs to be made in terms of the enhanced electro-optical coupling coefficient  $g_0$ . In principle, we can bypass these demanding requirements by using quantum teleportation protocol [47] with the assistance of a classical communication channel, which relies on continuous variable entanglement generation between microwave and optical modes by pumping the higher-frequency optical mode [3,48,49]. Assuming perfect homodyne detection, with our current noise measurement results and device parameters under optical drives of different powers, a continuous variable teleportation fidelity exceeding the "noncloning threshold" 2/3 [50] is possible if the electro-optical coupling rates  $g_0$ improves two orders of magnitude [40]. With the rapid development of cavity electro-optical systems based on different material platforms, these goals seem promising [22,25,27,28]. Reduced light-induced microwave noise could also help lower the requirement for  $g_0$ .

To summarize, we demonstrated efficient bidirectional MO conversion with a near-ground state integrated electro-optical converter and present a study of near-ground state microwave thermal excitations in a converter driven by strong pulsed optical drives. Dynamical noise study reveals that the microwave noise is limited by a fast responding effective bath caused by superconductor absorption of stray drive photons scattered from the chip-fiber interface. We show that, with practical improvements, microwave-to-optical quantum interface based on pulsed cavity-electro optical system is highly feasible.

## **ACKNOWLEGMENT**

This work is supported by ARO Grant No. W911NF-18-1-0020. The TWPAs used in this experiment are provided by IARPA and MIT Lincoln Laboratory. The authors also acknowledge partial supports from NSF (Grant No. EFMA-1640959) and the Packard Foundation. The authors thank Y. Sun, S. Rinehart, K. Woods, and M. Rooks for assistance in device fabrication.

W.F. and M.X. contributed equally to this work.

- [1] J. I. Cirac, P. Zoller, H. J. Kimble, and H. Mabuchi, Quantum State Transfer and Entanglement Distribution Among Distant Nodes in a Quantum Network, Phys. Rev. Lett. **78**, 3221 (1997).
- [2] H. J. Kimble, The quantum internet, Nature (London) 453, 1023 (2008).
- [3] C. Zhong, Z. Wang, C. Zou, M. Zhang, X. Han, W. Fu, M. Xu, S. Shankar, M. H. Devoret, H. X. Tang, and L. Jiang, Proposal for Heralded Generation and Detection of Entangled Microwave–Optical-Photon Pairs, Phys. Rev. Lett. 124, 010511 (2020).
- [4] L. Jiang, J. M. Taylor, A. S. Sørensen, and M. D. Lukin, Distributed quantum computation based on small quantum registers, Phys. Rev. A **76**, 062323 (2007).
- [5] C. Monroe, R. Raussendorf, A. Ruthven, K. R. Brown, P. Maunz, L.-M. Duan, and J. Kim, Large-scale modular quantum-computer architecture with atomic memory and photonic interconnects, Phys. Rev. A 89, 022317 (2014).
- [6] S. Blum, C. O'Brien, N. Lauk, P. Bushev, M. Fleischhauer, and G. Morigi, Interfacing microwave qubits and optical photons via spin ensembles, Phys. Rev. A 91, 033834 (2015).
- [7] D. Petrosyan, K. Mølmer, J. Fortágh, and M. Saffman, Microwave to optical conversion with atoms on a superconducting chip, New J. Phys. 21, 073033 (2019).
- [8] C. O'Brien, N. Lauk, S. Blum, G. Morigi, and M. Fleischhauer, Interfacing Superconducting Qubits and Telecom Photons Via a Rare-Earth-Doped Crystal, Phys. Rev. Lett. 113, 063603 (2014).
- [9] L. A. Williamson, Y.-H. Chen, and J. J. Longdell, Magneto-Optic Modulator with Unit Quantum Efficiency, Phys. Rev. Lett. 113, 203601 (2014).
- [10] R. Hisatomi, A. Osada, Y. Tabuchi, T. Ishikawa, A. Noguchi, R. Yamazaki, K. Usami, and Y. Nakamura, Bidirectional conversion between microwave and light via ferromagnetic magnons, Phys. Rev. B 93, 174427 (2016).
- [11] N. Zhu, X. Zhang, X. Han, C.-L. Zou, C. Zhong, C.-H. Wang, L. Jiang, and H. X. Tang, Waveguide cavity optomagnonics for microwave-to-optics conversion, Optica 7, 1291 (2020).
- [12] J. G. Bartholomew, J. Rochman, T. Xie, J. M. Kindem, A. Ruskuc, I. Craiciu, M. Lei, and A. Faraon, On-chip coherent microwave-to-optical transduction mediated by ytterbium in yvo4, Nat. Commun. 11, 3266 (2020).
- [13] J. Bochmann, A. Vainsencher, D. D. Awschalom, and A. N. Cleland, Nanomechanical coupling between microwave and optical photons, Nat. Phys. 9, 712 (2013).
- [14] R. W. Andrews, R. W. Peterson, T. P. Purdy, K. Cicak, R. W. Simmonds, C. A. Regal, and K. W. Lehnert, Bidirectional and efficient conversion between microwave and optical light, Nat. Phys. 10, 321 (2014).
- [15] I. Moaddel Haghighi, N. Malossi, R. Natali, G. Di Giuseppe, and D. Vitali, Sensitivity-bandwidth limit in a multimode optoelectromechanical transducer, Phys. Rev. Appl. 9, 034031 (2018).
- [16] A. P. Higginbotham, P. S. Burns, M. D. Urmey, R. W. Peterson, N. S. Kampel, B. M. Brubaker, G. Smith, K. W. Lehnert, and C. A. Regal, Harnessing electro-optic correlations in an efficient mechanical converter, Nat. Phys. 14, 1038 (2018).
- [17] M. Forsch, R. Stockill, A. Wallucks, I. Marinković, C. Gärtner, R. A. Norte, F. van Otten, A. Fiore, K. Srinivasan, and S. Gröblacher, Microwave-to-optics conversion using a mechan-

- ical oscillator in its quantum ground state, Nat. Phys. 16, 69 (2020).
- [18] C.-L. Zou, X. Han, L. Jiang, and H. X. Tang, Cavity piezomechanical strong coupling and frequency conversion on an aluminum nitride chip, Phys. Rev. A 94, 013812 (2016).
- [19] X. Han, W. Fu, C. Zhong, C.-L. Zou, Y. Xu, A. A. Sayem, M. Xu, S. Wang, R. Cheng, L. Jiang, and H. X. Tang, Cavity piezo-mechanics for superconducting-nanophotonic quantum interface, Nat. Commun. 11, 3237 (2020).
- [20] M. Mirhosseini, A. Sipahigil, M. Kalaee, and O. Painter, Superconducting qubit to optical photon transduction, Nature (London) 588, 599 (2020).
- [21] A. Rueda, F. Sedlmeir, M. C. Collodo, U. Vogl, B. Stiller, G. Schunk, D. V. Strekalov, C. Marquardt, J. M. Fink, O. Painter, G. Leuchs, and H. G. L. Schwefel, Efficient microwave to optical photon conversion: An electro-optical realization, Optica 3, 597 (2016).
- [22] W. Hease, A. Rueda, R. Sahu, M. Wulf, G. Arnold, H. G. Schwefel, and J. M. Fink, Bidirectional electro-optic wavelength conversion in the quantum ground state, PRX Quantum 1, 020315 (2020).
- [23] M. Tsang, Cavity quantum electro-optics. II. Input-output relations between traveling optical and microwave fields, Phys. Rev. A 84, 043845 (2011).
- [24] C. Javerzac-Galy, K. Plekhanov, N. R. Bernier, L. D. Toth, A. K. Feofanov, and T. J. Kippenberg, On-chip microwave-tooptical quantum coherent converter based on a superconducting resonator coupled to an electro-optic microresonator, Phys. Rev. A 94, 053815 (2016).
- [25] L. Fan, C.-L. Zou, R. Cheng, X. Guo, X. Han, Z. Gong, S. Wang, and H. X. Tang, Superconducting cavity electrooptics: A platform for coherent photon conversion between superconducting and photonic circuits, Sci. Adv. 4, eaar4994 (2018).
- [26] M. Soltani, M. Zhang, C. Ryan, G. J. Ribeill, C. Wang, and M. Loncar, Efficient quantum microwave-to-optical conversion using electro-optic nanophotonic coupled resonators, Phys. Rev. A 96, 043808 (2017).
- [27] T. P. McKenna, J. D. Witmer, R. N. Patel, W. Jiang, R. V. Laer, P. Arrangoiz-Arriola, E. A. Wollack, J. F. Herrmann, and A. H. Safavi-Naeini, Cryogenic microwave-to-optical conversion using a triply resonant lithium-niobate-on-sapphire transducer, Optica 7, 1737 (2020).
- [28] J. Holzgrafe, N. Sinclair, D. Zhu, A. Shams-Ansari, M. Colangelo, Y. Hu, M. Zhang, K. K. Berggren, and M. Lončar, Cavity electro-optics in thin-film lithium niobate for efficient microwave-to-optical transduction, Optica 7, 1714 (2020).
- [29] C. Wang, M. Zhang, X. Chen, M. Bertrand, A. Shams-Ansari, S. Chandrasekhar, P. Winzer, and M. Lončar, Integrated lithium niobate electro-optic modulators operating at cmos-compatible voltages, Nature (London) 562, 101 (2018).
- [30] S. Abel, F. Eltes, J. E. Ortmann, A. Messner, P. Castera, T. Wagner, D. Urbonas, A. Rosa, A. M. Gutierrez, D. Tulli, P. Ma, B. Baeuerle, A. Josten, W. Heni, D. Caimi, L. Czornomaz, A. A. Demkov, J. Leuthold, P. Sanchis, and J. Fompeyrine, Large pockels effect in micro- and nanostructured barium titanate integrated on silicon, Nat. Mater. 18, 42 (2019).
- [31] S. M. Meenehan, J. D. Cohen, S. Gröblacher, J. T. Hill, A. H. Safavi-Naeini, M. Aspelmeyer, and O. Painter, Silicon optome-

- chanical crystal resonator at millikelvin temperatures, Phys. Rev. A **90**, 011803(R) (2014).
- [32] S. M. Meenehan, J. D. Cohen, G. S. MacCabe, F. Marsili, M. D. Shaw, and O. Painter, Pulsed Excitation Dynamics of an Optomechanical Crystal Resonator Near Its Quantum Ground State of Motion, Phys. Rev. X 5, 041002 (2015).
- [33] K. S. Il'in, M. Lindgren, M. Currie, A. D. Semenov, G. N. Gol'tsman, R. Sobolewski, S. I. Cherednichenko, and E. M. Gershenzon, Picosecond hot-electron energy relaxation in nbn superconducting photodetectors, Appl. Phys. Lett. 76, 2752 (2000).
- [34] P. K. Day, H. G. LeDuc, B. A. Mazin, A. Vayonakis, and J. Zmuidzinas, A broadband superconducting detector suitable for use in large arrays, Nature (London) 425, 817 (2003).
- [35] M. Beck, M. Klammer, S. Lang, P. Leiderer, V. V. Kabanov, G. N. Gol'tsman, and J. Demsar, Energy-Gap Dynamics of Superconducting NbN Thin Films Studied by Time-Resolved Terahertz Spectroscopy, Phys. Rev. Lett. 107, 177007 (2011).
- [36] A. Kardakova, M. Finkel, D. Morozov, V. Kovalyuk, P. An, C. Dunscombe, M. Tarkhov, P. Mauskopf, T. M. Klapwijk, and G. Goltsman, The electron-phonon relaxation time in thin superconducting titanium nitride films, Appl. Phys. Lett. 103, 252602 (2013).
- [37] E. Zeuthen, A. Schliesser, A. S. Sørensen, and J. M. Taylor, Figures of merit for quantum transducers, Quantum Sci. Technol. 5, 034009 (2020).
- [38] C. Macklin, K. O'Brien, D. Hover, M. E. Schwartz, V. Bolkhovsky, X. Zhang, W. D. Oliver, and I. Siddiqi, A near-quantum-limited Josephson traveling-wave parametric amplifier, Science 350, 307 (2015).
- [39] M. Xu, X. Han, W. Fu, C.-L. Zou, and H. X. Tang, Frequency-tunable high-*Q* superconducting resonators via wireless control of nonlinear kinetic inductance, Appl. Phys. Lett. **114**, 192601 (2019).
- [40] See Supplemental Material at http://link.aps.org/supplemental/ 10.1103/PhysRevA.103.053504 for detailed description of device configuration, experimental setup, output line calibration, and teleportation fidelity calculation, which includes references [44,47,51–54].
- [41] T. Carmon, L. Yang, and K. J. Vahala, Dynamical thermal behavior and thermal self-stability of microcavities, Opt. Express 12, 4742 (2004).

- [42] M. Xu, X. Han, C.-L. Zou, W. Fu, Y. Xu, C. Zhong, L. Jiang, and H. X. Tang, Radiative Cooling of a Superconducting Resonator, Phys. Rev. Lett. 124, 033602 (2020).
- [43] Z. Wang, M. Xu, X. Han, W. Fu, S. Puri, S. M. Girvin, H. X. Tang, S. Shankar, and M. H. Devoret, Quantum microwave radiometry with a superconducting qubit, arXiv:1909.12295.
- [44] C. Weedbrook, S. Pirandola, R. García-Patrón, N. J. Cerf, T. C. Ralph, J. H. Shapiro, and S. Lloyd, Gaussian quantum information, Rev. Mod. Phys. 84, 621 (2012).
- [45] M. M. Wolf, D. Pérez-García, and G. Giedke, Quantum Capacities of Bosonic Channels, Phys. Rev. Lett. 98, 130501 (2007).
- [46] A. S. Holevo and R. F. Werner, Evaluating capacities of bosonic Gaussian channels, Phys. Rev. A **63**, 032312 (2001).
- [47] S. L. Braunstein and H. J. Kimble, Teleportation of Continuous Quantum Variables, Phys. Rev. Lett. 80, 869 (1998).
- [48] S. Barzanjeh, M. Abdi, G. J. Milburn, P. Tombesi, and D. Vitali, Reversible Optical-To-Microwave Quantum Interface, Phys. Rev. Lett. 109, 130503 (2012).
- [49] A. Rueda, W. Hease, S. Barzanjeh, and J. M. Fink, Electro-optic entanglement source for microwave to telecom quantum state transfer, npj Quantum Inf. 5, 108 (2019).
- [50] F. Grosshans and P. Grangier, Quantum cloning and teleportation criteria for continuous quantum variables, Phys. Rev. A 64, 010301(R) (2001).
- [51] T. Lindström, J. E. Healey, M. S. Colclough, C. M. Muirhead, and A. Y. Tzalenchuk, Properties of superconducting planar resonators at millikelvin temperatures, Phys. Rev. B 80, 132501 (2009).
- [52] A. J. Annunziata, D. F. Santavicca, L. Frunzio, G. Catelani, M. J. Rooks, A. Frydman, and D. E. Prober, Tunable superconducting nanoinductors, Nanotechnol. 21, 445202 (2010).
- [53] D. Niepce, J. Burnett, and J. Bylander, High kinetic inductance NbN nanowire superinductors, Phys. Rev. Appl. 11, 044014 (2019).
- [54] J. Gao, M. Daal, A. Vayonakis, S. Kumar, J. Zmuidzinas, B. Sadoulet, B. A. Mazin, P. K. Day, and H. G. Leduc, Experimental evidence for a surface distribution of two-level systems in superconducting lithographed microwave resonators, Appl. Phys. Lett. 92, 152505 (2008).